International Journal of Microwave and Wireless Technologies

cambridge.org/mrf

A comparison of near-field to far-field transformation techniques for use with industrial multi-axis robotic antenna measurement systems

S.F. Gregson[1,2], C.G. Parini[2], D. Lewis[3] and W. Cooper[3]

[1]Next Phase Measurements LLC, Garden Grove, CA, USA; [2]School of Electronic Engineering & Computer Science, Queen Mary University London, London, UK and [3]The Boeing Company Test & Evaluation – Electromagnetics Seattle, Washington Boeing, Seattle, USA

Research Paper

Cite this article: Gregson SF, Parini CG, Lewis D, Cooper W (2025) A comparison of near-field to far-field transformation techniques for use with industrial multi-axis robotic antenna measurement systems. *International Journal of Microwave and Wireless Technologies*, 1–10. https://doi.org/10.1017/S1759078725000157

Received: 3 September 2024
Revised: 20 January 2025
Accepted: 26 January 2025

Keywords:
current elements; cylindrical; gain; Kirchhoff–Huygens; planar; plane-polar; plane-rectilinear; spherical

Corresponding author: Stuart Gregson; Email: stuart.gregson@qmul.ac.uk

Abstract

This invited, extended, paper compares and contrasts a number of different near-field (NF) to far-field (FF) transformation algorithms that can be used for the purpose of processing NF data acquired using multi-axis industrial robots. The merits and limitations of these various, commonly encountered algorithms are highlighted with comparison FF data presented across a frequency range spanning 3–15 GHz. Crucially, the paper explores the viability of using mixed mode acquisition geometries when performing antenna gain measurements where, prior to this work, several of the transforms yielded different transform gains, and electrical lengths. Here, we verify that at 8 GHz and above, where truncation effects were minimal, for a circa 30 dBi gain (at 8 GHz) test antenna the FF peaks were in agreement to better than ± 0.02 dB, at 3σ irrespective of the acquisition geometry and transform algorithm used. In this invited, extended work, the existing simulation results are augmented with experimental results obtained from planar and spherical NF measurements of a pyramidal horn taken using a dual robotic antenna measurement system and a consistent distributed RF subsystem.

Introduction

Electromagnetic near-field (NF) to far-field (FF) transformations are generally used to calculate the FF antenna pattern of some radiator from an acquisition of a sufficiently large number of NF measurements. Early transformation algorithms were largely restricted to considering canonical geometries such as spheres, cylinders, or planes. These were typically implemented employing fast Fourier transform based algorithms which were extremely efficient, robust, and numerically very accurate. Such direct inversion techniques included probe compensation, required only the measurement of quantities proportional to the electric fields, and utilized mode orthogonality of the field expansions in these special coordinate systems [1–4]. This limited them to certain fixed measurement geometries, with regularly spaced sample locations with appropriately, and very carefully, oriented probes where in some cases those probes also needed to demonstrate certain symmetries. As a result of this, most NF measurement facilities were designed and constructed to adhere with these requirements and have been largely responsible for underpinning the reliability and tremendous success of the NF measurement approach.

More recently, an alternative approach has gained traction. Here, greater flexibility in terms of the representation of the antenna and acquisition type can be obtained using an inverse equivalent source method. These tend to utilize a discrete set of surface current densities defined on a meshed surface surrounding (or sometimes just in front of) the antenna as a spatial representation of the source. Here, a discrete linear system of equations is set up and then solved, for example, as a pseudoinverse solution [1, 4, 5]. In this paper, we examine several different field transformation algorithms highlighting their utility for use in modern industrial multi-axis robotic based antenna measurement systems. An earlier version of this paper was presented at the 18th European Conference on Antennas and Propagation (EuCAP 2024) and was published in its proceedings [6]. This invited paper comprises an extended version of that original work which, unlike the original, includes further experimental confirmation to the proposed measurement method.

A modern industrial multi-axis robotic based antenna measurement system is shown in Fig. 1, where acquisitions can be taken in a variety of different modes with the same Radio Frequency (RF) subsystem and Antenna Under Test (AUT). The purpose was twofold, firstly to verify the reliability of the respective transforms and secondly to confirm the consistency of amplitude and phase normalization between them. The transformation approaches examined were (1) Kirchhoff–Huygens formula [1, 4] and (2) current elements formula [4, 7]

Figure 1. Dual multi-axis industrial robotic antenna measurement system, picture courtesy of Boeing.

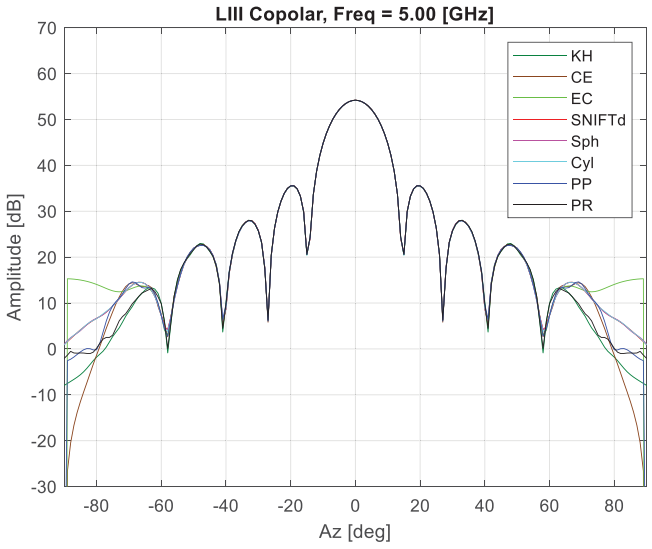

Figure 2. Copolar far-field azimuth amplitude pattern.

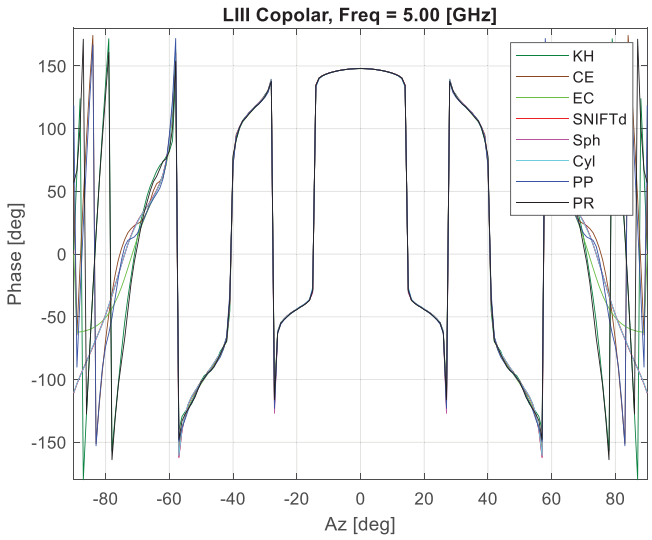

Figure 3. Copolar far-field azimuth phase pattern.

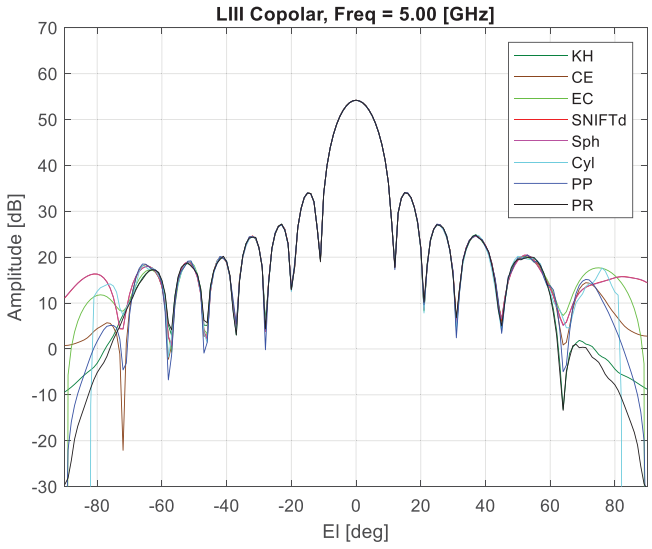

Figure 4. Copolar far-field elevation amplitude pattern.

which are both physical optic based field propagation algorithms, (3) equivalent currents method [4, 5] which is a variation on a method-of-moments based approach, (4) classicalspherical mode expansion based transform using SNIFTd [8], (5) an equivalent proprietary spherical mode expansion [1], (6) a proprietary cylindrical mode expansion based algorithm [1, 9], (7) a proprietary accelerated plane-polar based transform [4] and finally, (8) a proprietary plane-rectilinear based transform [4].

These eight completely different transformation approaches can be used to provide the equivalent FF pattern of some radiator from NF data, acquired over an appropriate two-dimensional surface providing the following remain unchanged: (1) test antenna, (2) frequency, (3) input power, (4) loss through the RF subsystem, i.e. the losses through the guided wave path, Intermediate Frequency (IF) bandwidth, etc., (5) match in the feed, (6) unimportant spherical phase factor and inverse distance terms are divided out of the FFs, (7) stable consistent antenna gain via transform normalization through the NF to FF post-processing software.

With regards to item 6, expressly we mean that, for a positive suppressed time dependency, the factor,

$$\frac{e^{-jk_0 r}}{k_0 r} \tag{1}$$

is divided out of the computed FF patterns where k_0 is the wavenumber. This suppresses the radial dependence of the transformed fields, meaning that with this suppressed in the FF region, one would see the same amplitude and phase patterns as the radial distance changes. For example, we may take the planar case as it is mathematically perhaps the simplest to consider. The angular spectrum can be obtained directly from the sampled tangential NF components using the FF peak through the following equation [3, 6],

$$\underline{F_T}\left(k_x, k_y\right) = \frac{4\pi}{\lambda^2} e^{j\frac{\pi}{2}} \int_{-\infty}^{\infty}\int_{-\infty}^{\infty} \underline{E_T}\left(x, y, z=0\right) e^{j\left(k_x x + k_y y + k_z z\right)} dxdy \tag{2}$$

https://doi.org/10.1017/S1759078725000157 Published online by Cambridge University Press

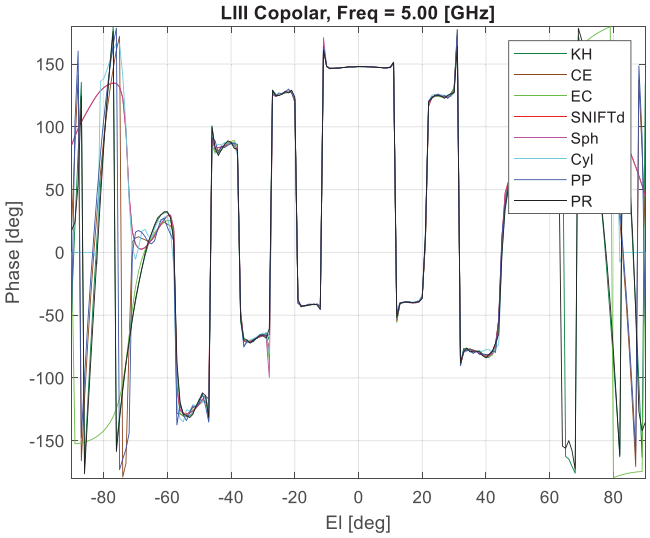

Figure 5. Copolar far-field elevation phase pattern.

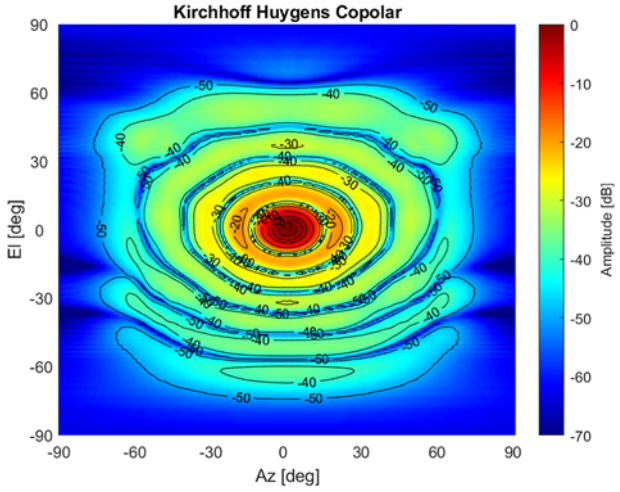

Figure 6. Kirchhoff–Huygens transform copolar.

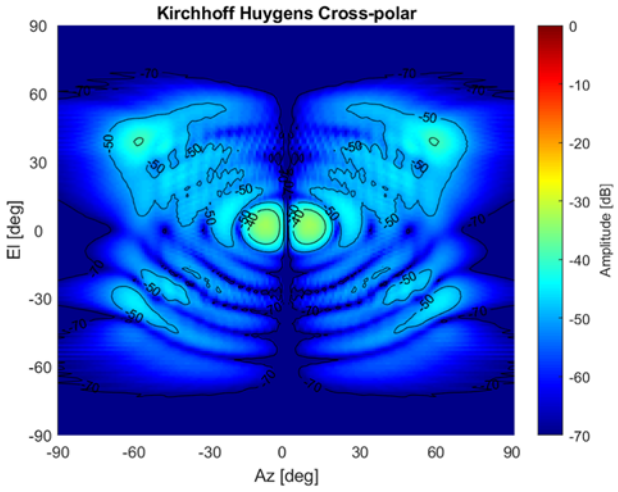

Figure 7. Kirchhoff–Huygens transform cross-pol.

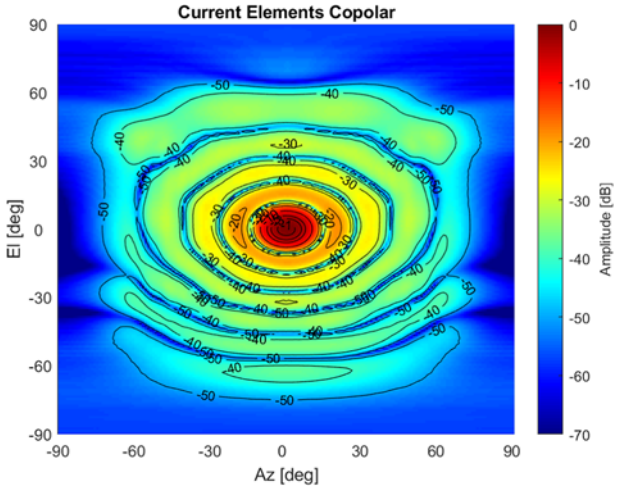

Figure 8. Current elements transform copolar.

Here, the inclusion of the factor $4\pi/\lambda^2$ is required to ensure that the planar transform has a gain that is equivalent to that of the cylindrical, spherical, etc., transforms. Similarly, the inclusion of the 90° phase change, i.e. the complex exponential factor in front of the integral, is required purely to provide consistency with the FF phase pattern provided by other transforms. Thus, for the same test antenna, input power, frequency, match, etc., the FF amplitude and phase peak values should be the same for each transform. For industrial multi-axis based antenna measurement systems, this is particularly important as a single system can be used to acquire data using one of several modes with users wishing to be able to directly compare FF measurements irrespective of the measurement mode used, and this of course includes the measurement of FF gain.

Mixed acquisition mode gain measurements

In many cases, the gain of an antenna is obtained using the gain-substitution method [1–4]. This method transfers the gain of a known standard to an unknown test antenna and can, when omitting the mismatch correction factor required when measuring IEEE gain, be expressed as,

$$G_{\mathrm{AUT}} = \left(E_{\mathrm{AUT}}^{\mathrm{Peak}} - E_{\mathrm{SGA}}^{\mathrm{Peak}}\right) + G_{\mathrm{SGA}} \tag{3}$$

Here, G_{AUT} is the gain of the AUT, G_{SGA} is the gain of the standard gain antenna (SGA) which is assumed known a priori, $E_{\mathrm{AUT}}^{\mathrm{Peak}}$ is the FF pattern peak of the AUT, and $E_{\mathrm{SGA}}^{\mathrm{Peak}}$ is the FF pattern peak of the SGA where all of these quantities are in dB (i.e. logarithmic) form.

Usually, assumption 7 above, the transform normalization, is guaranteed by virtue of the same test system (and therefore geometry and transformation algorithm) being used to acquire both the AUT and the SGA. However, as expounded above, the recent proliferation of NF test systems employing multi-axis industrial robots within their great flexibility in their positioning sub-systems has resulted in the need to acquire test antennas, which for example could be low gain, using different acquisition geometries to SGAs, which are generally medium to higher gain. In this case, different NF to FF transformation algorithms may be used to process the SGA data to the AUT data and thus, not only the stability of the transformation but also the inherent

https://doi.org/10.1017/S1759078725000157 Published online by Cambridge University Press

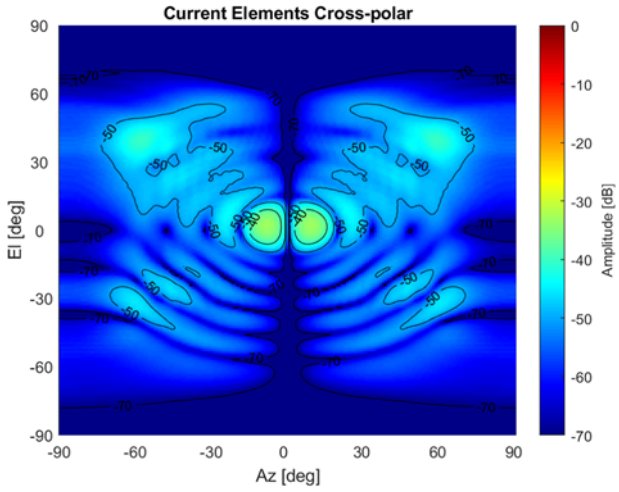

Figure 9. Current elements transform cross-pol.

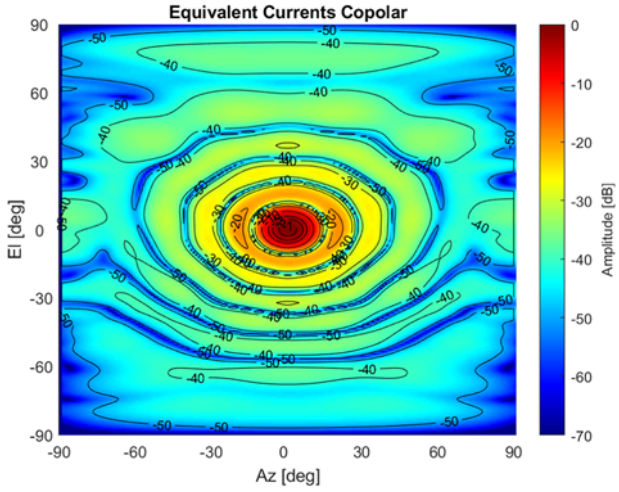

Figure 10. Equivalent currents transform copolar.

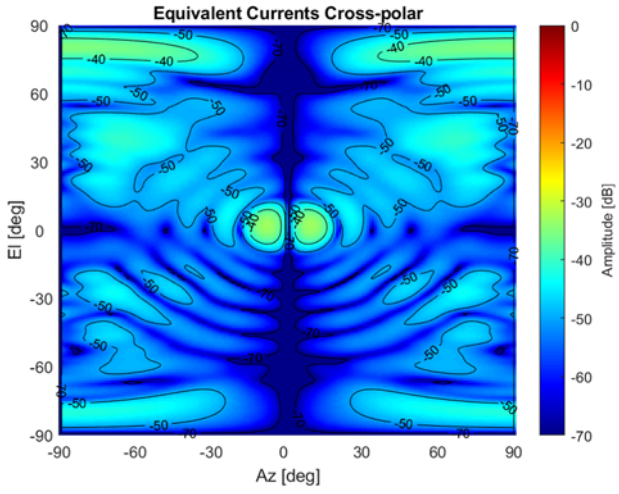

Figure 11. Equivalent currents transform cross-pol.

gain through the transform becomes crucial if the application of equation (3) is to be reliable since $E_{\mathrm{AUT}}^{\mathrm{Peak}}$ and $E_{\mathrm{SGA}}^{\mathrm{Peak}}$ depend upon the respective transform normalizations. Although providing a

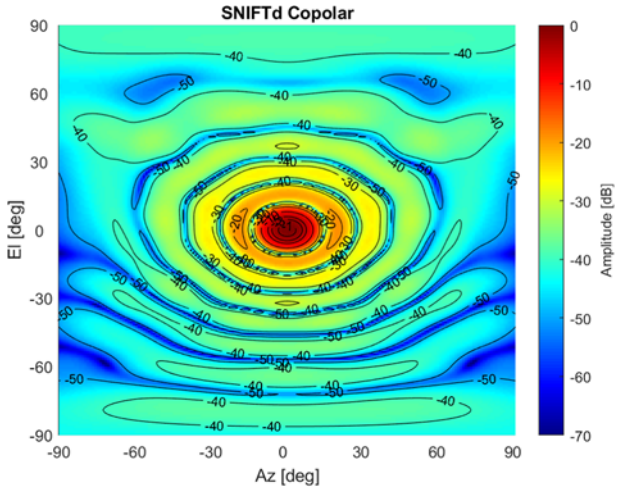

Figure 12. SNIFTd transform copolar.

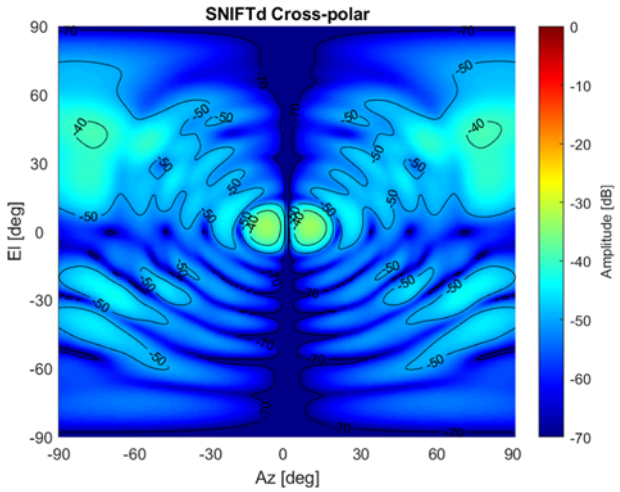

Figure 13. SNIFTd transform cross-pol.

stable gain is typically verified as part of the software validation procedure, as this ensures independence from the details of the sampling interval and sample spacing, the relative transform normalizations are not typically cross-correlated within the validation activity as this has not historically been of interest or concern because both AUT and SGA were measured using the same technique. It is noted here that questions relating to establishing the commonality of respective RF network losses through the guided wave paths are outside the scope of the present study. Furthermore, we have ignored mismatch correction [1] which would need to be compensated for if highly accurate gain measurements are required as this too is independent of the transforms gain and electrical length. A second method for computing the FF gain of an antenna is by means of the direct cable connection method. As all of the transforms provide the same gain, and electrical path length, the same direct cable connection formula may be used with FF data obtained from any of these transforms without further modification. Thus, the gain of an antenna may be determined by the direct gain calculation using,

$$G_{\mathrm{AUT}} = E_{\mathrm{AUT}}^{\mathrm{Peak}} - (G_{\mathrm{Probe}} + \text{Bypass Measurement}) \qquad (4)$$

https://doi.org/10.1017/S1759078725000157 Published online by Cambridge University Press

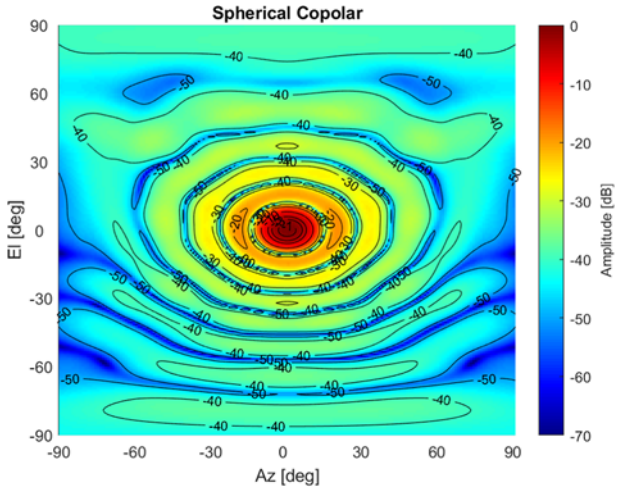

Figure 14. Spherical transform copolar.

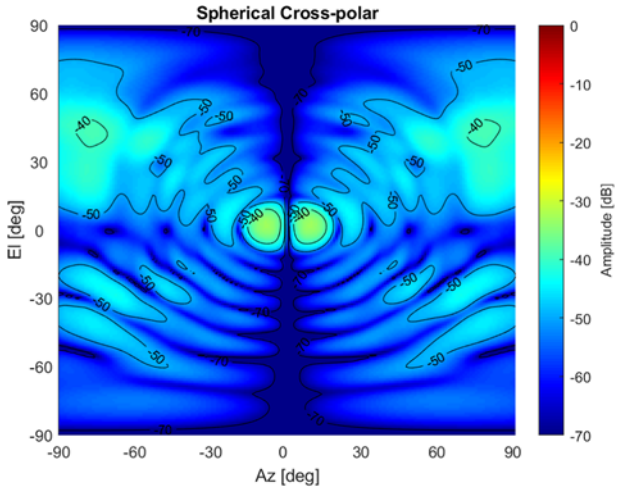

Figure 15. Spherical transform cross-pol.

Here, $E_{\mathrm{AUT}}^{\mathrm{Peak}}$ is the FF pattern peak of the AUT, G_{Probe} is the gain of the NF probe which is assumed known a priori, and the bypass measurement is a way of calibrating out the effects of cable losses within the RF sub-system where all of the values are in dB form. The bypass measurement involves connecting the cable that went to the AUT with the cable that was connected to the probe and recording the signal in dB. Any loss resulting from the addition of a connector would need to be extracted from this measurement as a network adjustment. Note, again we have ignored mismatch connection here which would need to be compensated for if highly accurate gain measurements are required. Historically, many transforms do *not* have the same transform normalization and as such it is *not* normally possible to use equation (4) in this way without further modification.

The approach used for the validation campaign was to simulate NF measured data for a given antenna for each frequency, for fixed input power, etc., for each of the NF acquisition geometries: plane-rectilinear, plane-polar, cylindrical, and spherical. The various acquisition geometries will introduce artefacts resulting from the truncation differences between the respective techniques. However, these effects should be minimized when comparing the respective FF pattern boresight peaks, and as the electrical size of the AUT increases. The comparison was also repeated over a band of frequencies to insure the generality of the result.

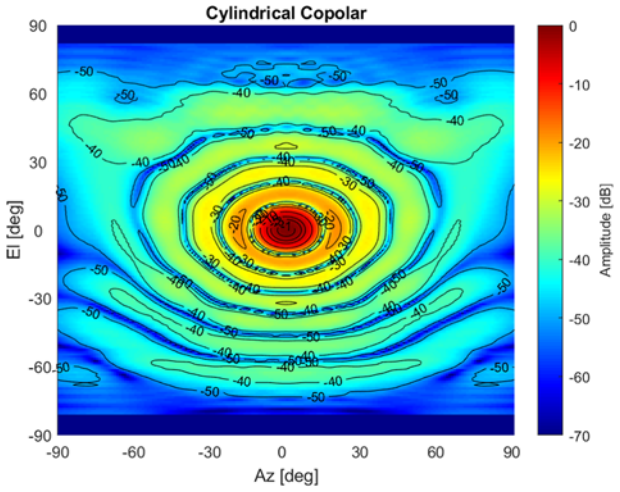

Figure 16. Cylindrical transform copolar.

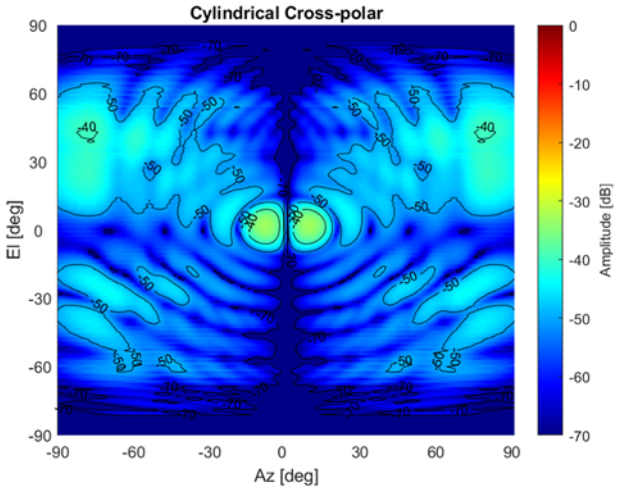

Figure 17. Cylindrical transform cross-pol.

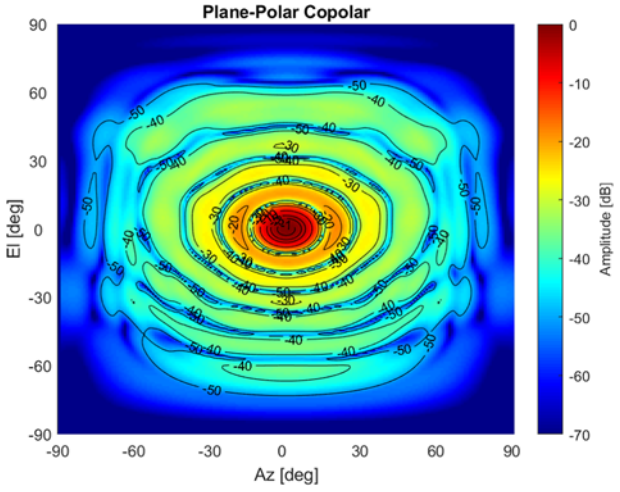

Figure 18. Plane-polar transform copolar.

https://doi.org/10.1017/S1759078725000157 Published online by Cambridge University Press

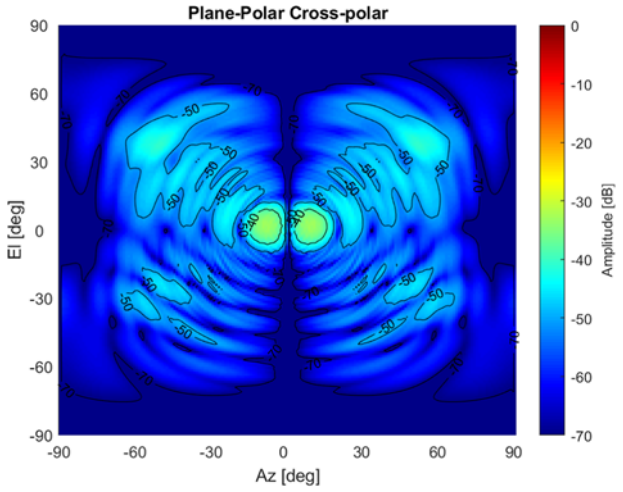

Figure 19. Plane-polar transform cross-pol.

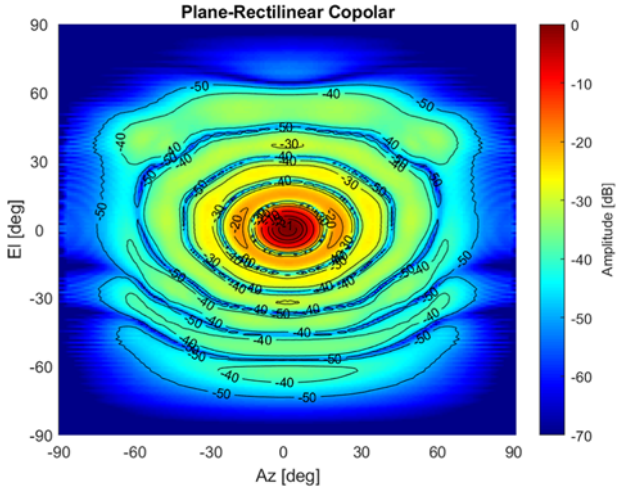

Figure 20. Plane-rectilinear transform copolar.

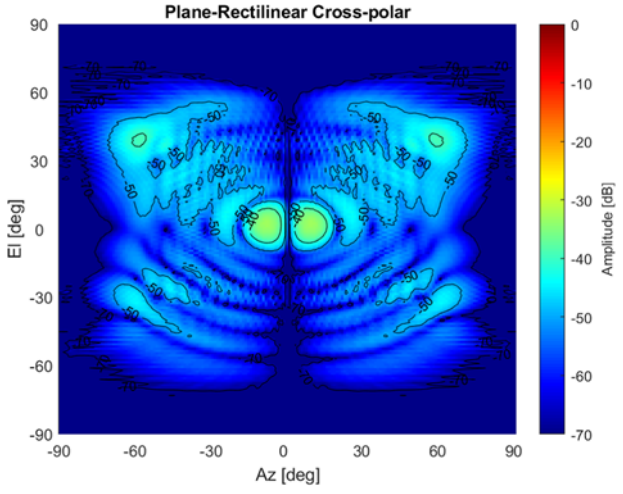

Figure 21. Plane-rectilinear transform cross-pol.

Simulation

NF measured data of a single offset reflector antenna was simulated from 3 to 15 GHz using a physical-optics based algorithm. The

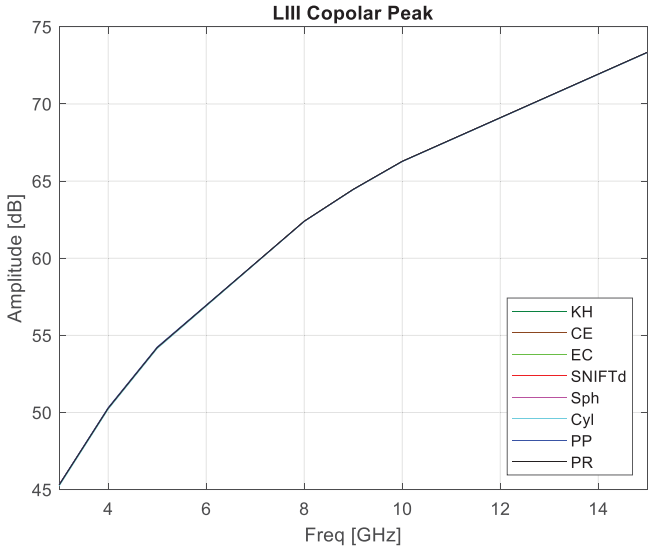

Figure 22. Plot of copolar pattern peak as a function of frequency for several different near-field to far-field transform algorithms.

Table 1. Comparison of transform gain and electrical length at 5 GHz on boresight

Transform type	Amplitude (dB)	Phase (deg)
Kirchhoff–Huygens	54.20	147.9
Current elements	54.20	147.9
Equivalent currents	54.20	147.9
SNIFTd	54.20	147.9
Spherical	54.20	147.9
Cylindrical	54.19	147.9
Plane-polar	54.25	148.1
Plane-polar (larger disk)	54.20	148.1
Plane-rectilinear	54.20	147.9
Plane-rectilinear (disk)	54.21	148.0

NF data were produced on a plane, a cylinder, and a sphere while keeping all parameters for the antenna fixed. This was repeated across a band of frequencies. Both electric (E) and magnetic (H) fields were produced so that the Kirchhoff–Huygens formula (which required both E- and H-fields) and the current elements formula (which required just H-fields) could be used. All other transforms required just the E-fields. To illustrate this, the 5 GHz NF data were transformed to the FF using the eight different transforms and can be seen plotted in Fig. 2 as an azimuth amplitude cut where *no* normalization has been applied, and where the unimportant spherical phase factor and inverse distance terms have been divided out of the FFs. Here, and in all other plots in this paper, the following acronyms have been used: KH is Kirchhoff–Huygens formula, CE is current elements formula, EC is the equivalent currents method, SNIFTd denotes Ticra's proprietary spherical NF to FF program, Sph is a proprietary spherical mode expansion transform, Cyl is a proprietary cylindrical transform, PP is a proprietary plane-polar transform, and lastly PR is a proprietary plane-rectilinear transform. All of these modal transforms assumed the

https://doi.org/10.1017/S1759078725000157 Published online by Cambridge University Press

Table 2. Comparison of transform directivity at 5 GHz

Transform type	Directivity (dBi) Forward half-space
SNIFTd	25.16
Spherical	25.16
Cylindrical	25.16
Kirchhoff–Huygens	25.18
Current elements	25.18
Equivalent currents	25.16
Plane-rectilinear	25.17
Plane-rectilinear (truncated to NF disk)	25.19
Plane-polar	25.20
Plane-polar (larger NF disk diameter)	25.16

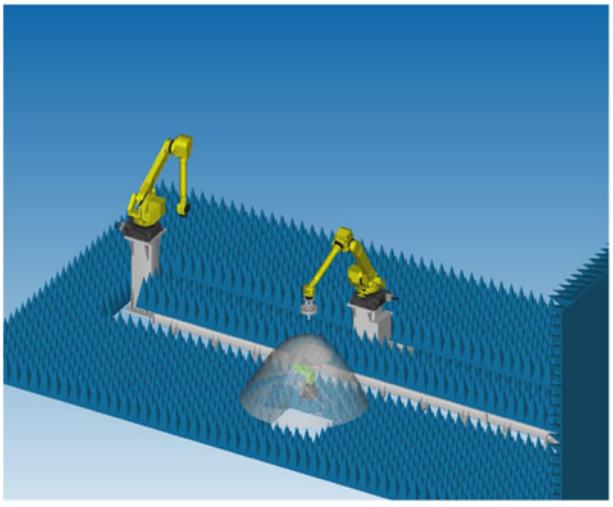

Figure 23. Illustration of the dual six-axis robotic antenna measurement system shown with AUT as a planar array covered by a radome.

use of an electric infinitesimal Hertzian dipole for the input (NF sampling) probe.

Although not shown due to the pressures of space, additionally each of the planar, cylindrical, and spherical transforms were run using the FF pattern of an x- and y-axis orientated Hertzian dipole probe, and almost identical FF pattern normalization were obtained, i.e. the differences were far smaller than the next smallest term in the typical facility uncertainty budget. This is examined in more detail below. When reviewing these results, it is important to note several of these transforms have different native FF coordinate systems. Thus, 16 point bi-cubic convolution interpolations were used to re-tabulate the patterns. This was unavoidable and will introduce some degree of approximation. Fig. 3 presents an FF azimuth phase plot where again no normalization has been applied. As is evident from these figures, and the equivalent elevation cuts presented in Figs. 4 and 5 show that all eight transforms are in very encouraging agreement in amplitude and phase over the FF valid region as determined by the amount of truncation incurred in the NF. Some differences will result from the interpolation that is needed to present all of these patterns tabulated in the same coordinate system. However, this error should be small.

When comparing these FF cuts, it is important to take into account the differences that measurement truncation has on each of these FF patterns. For the planar (and cylindrical) cases, the valid angle [1, 4] is *circa* 60° for these simulated measurements. Thus, we can expect to see differences in the FF pattern for these simulated measurements. As the frequency increases, the directivity of the offset reflector antenna increases and so the finitely large acquisition intervals sample a larger proportion of the radiated field and as such the truncation error will decrease. Note, this can be seen more easily below where we examine the respective pattern peaks. Here, the spherical cases (red and magenta traces) are truncation free. The cylindrical azimuth cut (cyan trace) is free from the first order truncation effect but will suffer first order truncation in the elevation plane. The plane rectilinear (black trace) and plane-polar (blue trace) cases will exhibit truncation in both the azimuth and elevation cuts but as the plane rectilinear FF data are derived from a square acquisition and the plane-polar data are derived from a circular disk, some differences will be seen, although these will be small. For example, the RMS dB difference level between the respective spherical mode expansion based transforms was better than −87 dB, which is far below any other term within the facility level uncertainty budget. The KH (dark green trace), CE (purple trace), and EC (light green trace) FF data were derived from plane-rectilinear NF data so each will contain truncation artefacts. However, the way in which this is manifested will be different from case to case as the underlying assumptions and boundary conditions are different in each formulation.

By way of a further comparison, Figs. 6–21 present the Ludwig 3 [1, 4], copolar and cross-polar FF, 5 GHz, amplitude patterns, plotted over the forward half-space in the form of a false-color checkerboard plot that for consistency have been normalized by the same factor so that the elemental peak of the copolar SNIFTd pattern was exactly 0 dB. From inspection of these patterns, both copolar and cross-polar, we can see that they are all in very encouraging agreement. Some differences can be seen in the wideout side-lobe regions, e.g. beyond ∼60° where truncation effects and differences in the respective boundary conditions impact the patterns.

For example, the plane-wave spectrum based representations underreport the wideout pattern levels where as the EC method overreports the fields. Neither is correct, with these artefacts arising from their formulation. However, it is important to recognize these phenomena, and be sensitive to their impacts on the calculation of directivity by way of pattern integration.

By way of a further comparison, Fig. 22 presents a comparison of the FF peak amplitude plotted as a function of frequency which has been evaluated from 3 GHz to 15 GHz. The same nomenclature and key has been used here as was employed in Figs. 2–5.

Clearly, all of the FF elemental peaks are in very good agreement. However, above 8 GHz, the effects of truncation are greatly reduced, and the differences between the respective FF pattern peaks reduce to circa 0.02 dB at two standard deviations. At these frequencies, the uncertainty on a typical gain standard may be as much as ±0.5 dB which is significantly larger than the differences observed here and which, as was noted above, is an artefact of truncation. Table 1 presents a comparison of the peak amplitudes and phase values for each of these transforms for the 5 GHz case.

From inspection of Table 1, we can see that the amplitude and phase values are in very good agreement. The plane-polar transform is in the poorest agreement. However, by increasing the diameter of the NF acquisition, the FF comes into agreement with the other transforms. Interestingly, by truncating the planar-rectilinear NF to a disk of the same size as the

https://doi.org/10.1017/S1759078725000157 Published online by Cambridge University Press

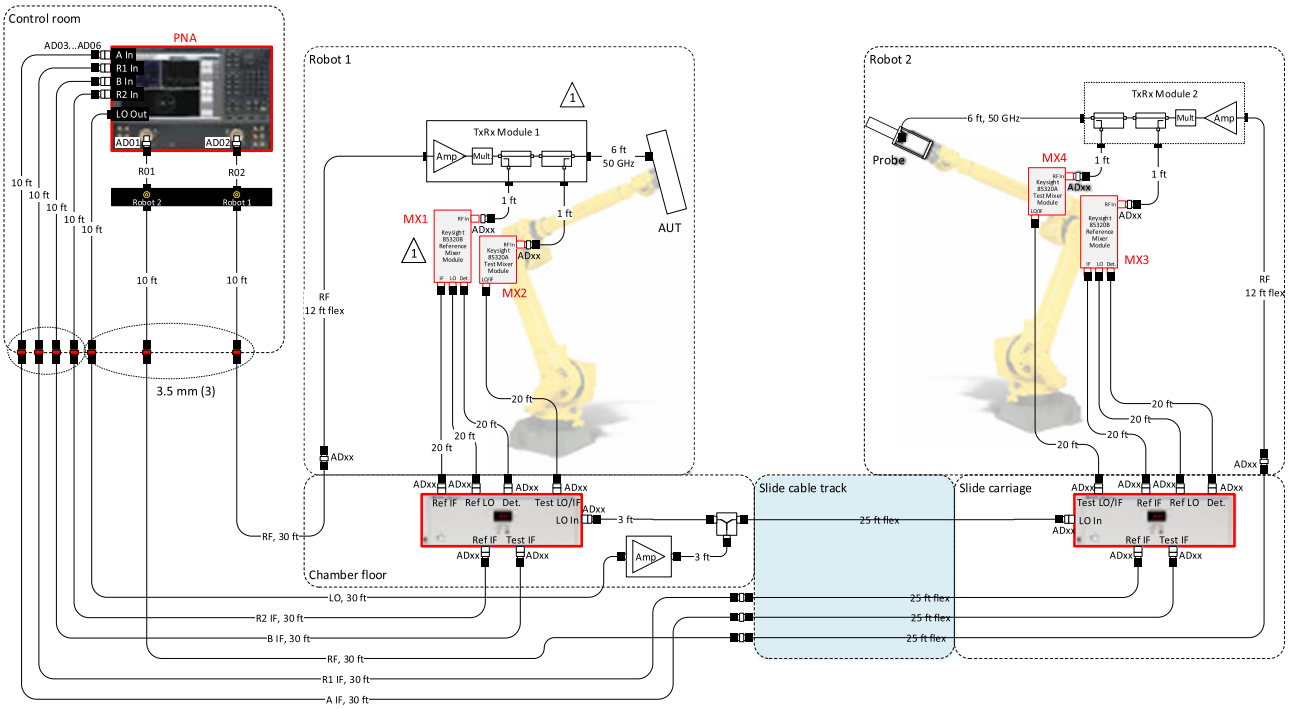

Figure 24. RF subsystem of dual robotic antenna measurement system.

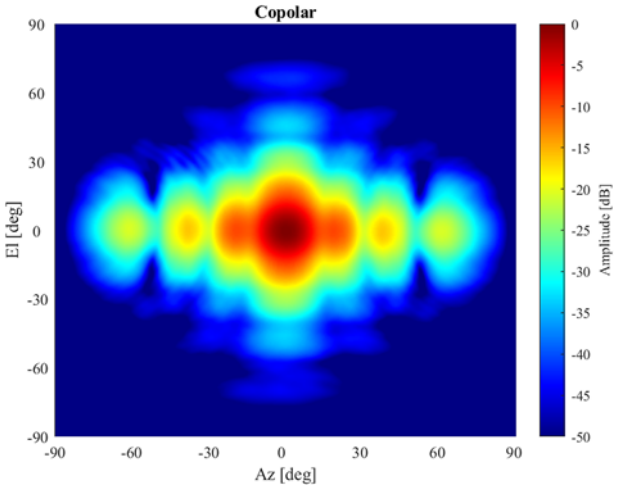

Figure 25. Far-field copolar pattern of SGH acquired using a PNF measurement mode.

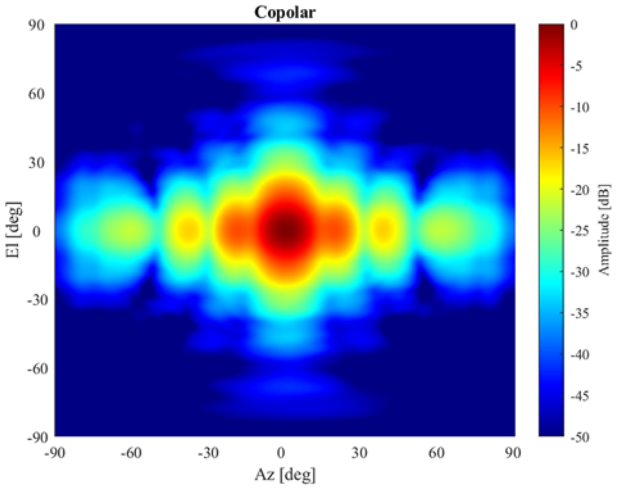

Figure 26. Far-field copolar pattern of SGH acquired using an SNF measurement mode.

plane-polar simulated measurement moves that peak into closer agreement with the plane-polar case. It is worth noting that the plane-polar transform and a DFT based transform were in agreement at circa −150 dB so this difference is not believed to be a fault of the transform per se, but rather a difference in the way truncation impacts the transformed FFs [4, 10]. Thus, we see that the first and second order truncation effects [1, 4] are the primary cause for FF differences. As a final comparison, Table 2 contains a comparison of the directivities obtained from an FF pattern integration that was performed on the FFs where, for the purpose of consistency, the patterns were limited to the forward half-space only.

From inspection of Table 2, we see that all of the reported directivities were in agreement to within 0.04 dBi at 5 GHz. The agreement improved at higher frequencies as the electrical size of the antenna increased, and the proportion of the radiated field that passes through the NF sampling interval increased so that truncation effects decreased.

Experimental confirmation of consistency of NF to FF transform gains

So that the stable transform normalization could be verified experimentally a new dual robotic antenna measurement system was utilized to take the NF data. This industrial robotic based antenna measurement system is installed within a screened, environmentally controlled 12.5 × 8 × 5 m [41′ × 26′ × 17′] (L × W × H)

https://doi.org/10.1017/S1759078725000157 Published online by Cambridge University Press

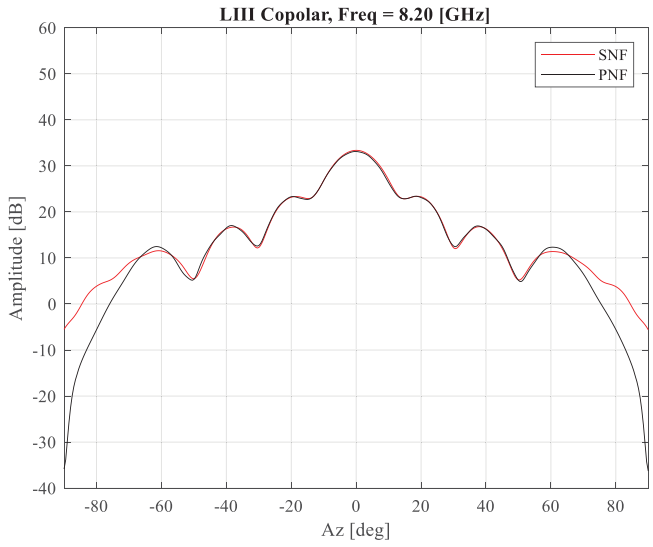

Figure 27. Far-field azimuth cut comparing SGH acquired using SNF, red trace, and planar measurement modes, black trace.

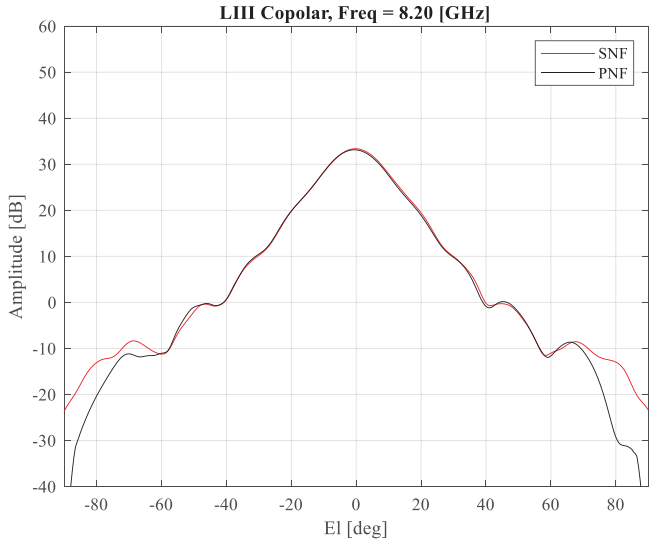

Figure 28. Far-field elevation cut comparing SGH acquired using SNF, red trace, and planar measurement modes, black trace.

anechoic chamber which is lined with 0.60 m [24″] pyramidal absorber. One of the two multi-axis industrial robots is fixed, with the other mounted on top of a 9 m [30′] linear translation stage.

Each of the multi-axis robots are installed on pedestals so that the AUT and probe are positioned toward the centerline of the anechoic chamber. This can be seen presented in Fig. 23 with the stationary robot shown to the left and the moving robot on the right. Here the AUT is a planar array antenna covered by a radome. The system shown here provides 14 separate computer-controlled axes. This is formed from the two 6-axis robots, the linear axis under the moving robot and an AUT azimuth stage installed on the chamber floor. This azimuth stage is used as a ϕ-axis of the spherical near-field (SNF) positioning system.

The implementation of an RF subsystem for this sort of complex robotic antenna measurement system can be challenging as it must be reconfigurable adapting to a range of very diverse measurement scenarios without sacrificing RF performance. Due to the very wide range of motion afforded by a multi-axis robotic system, cable management and phase stability due to flexure within the guided wave path can be problematic. Furthermore, the large physical size and increased length of that guided wave path generally results in the adoption of a distributed RF-subsystem which is needed to manage the power budget, and sensitivity requirements, required by the measurement system. The RF subsystem deployed can be seen presented in Fig. 24. Crucially, for this study, there is no need to reconfigure the RF subsystem or reconnect the AUT or probe between measurements, even when those measurements are of a different NF acquisition geometry [11].

Thus, when taking the NF data, exactly the same RF sub-system could be used for the two different acquisition geometries where it was possible to maintain the guided wave path, power levels, Intermediate Frequency Band Width (IFBW), cable lengths, attenuation, amplification, etc. For this study, an X-band pyramidal standard gain horn (SGH) was acquired in both spherical and planar modes using a WR90 rectangular open-ended waveguide probe. The measured data were transformed to the FF using the equalized planar and spherical transforms presented above with the FF patterns being plotted without further normalization. In a gain measurement, this would provide the value for $E_{\mathrm{SGA}}^{\mathrm{Peak}}$ in equation (3). Clearly, the two acquisitions are very different in form. The SNF measurement was taken with a measurement radius of 1.0 m, with spherical NF data being acquired over the forward hemisphere. Conversely, the planar acquisition was taken with an AUT-to-probe separation of 0.18 m with planar data being taken out to ± 1 m in both the x- and y-axes. The different range lengths were compensated for within the probe compensation portion of the respective transformation algorithms, as was the differing probe pattern effects resulting from the difference probe orientations in the two measurement modes. Figure 25 presents a false color, checkerboard plot of the copolar FF pattern obtained from the Planar Near-Field (PNF) measurement while Fig. 26 shows an equivalent plot for the SNF measurement case.

From inspection of these plots, we can see that the patterns are in good general agreement with greater truncation effects being present in the PNF measurement [1, 4]. By way of a further comparison, Figs. 27 and 28 contain comparison plots of the copolar cardinal cuts. Here, the red traces denote the spherical measurements whilst the black trace denotes the planar measurements.

From inspection of the respective FF data, the un-normalized FF peaks were different by *circa* 0.24 dB which, as was shown in "Simulation" section, is larger than the 0.02 dB difference that can be attributed to the difference between the respective NF to FF transforms. However, these measurements were taken somewhat opportunistically and were separated in time from one another by a few days. Additionally, the pyramidal horn was remounted between measurements. Thus, although far from reference measurements, these are sufficient to be able to confirm that the transform normalizations have been equalized to a point where the transform component of the gain uncertainty budget is much smaller than many of the other terms in the range gain assessment. Of these, range reflections, AUT-to-probe multiple reflections and truncation can be expected be some of the larger terms and they will manifest themselves very differently between the respective measurement modes.

Summary and conclusions

This paper presents the results of a recent study that obtained consistent gain and electrical length for eight different field

https://doi.org/10.1017/S1759078725000157 Published online by Cambridge University Press

transformation formulas. Initially, most of the transform normalizations and electrical lengths varied between transforms due to differences within the respective derivations and implementations. However, it was found that these could be equalized, with changes mainly being related to the translation of origins formula as required by the probe compensation formula and aligned with equation (1) and Ref [8]. Here, the spherical, cylindrical, and planar algorithms were intended for use with industrial multi-axis robotic antenna measurement systems and provision of consistent FF data, irrespective of the acquisition geometry, NF probe, and transform algorithm used is desirable and permits both gain substitution and direct cable connection techniques to be used irrespective of whether the SGH and AUT were acquired using the same or different geometries. Associated uncertainty arising between different NF measurement techniques is primarily due to the degree of truncation suffered during the measurement, with the difference in the transform gains being negligible for all practical purposes. The planned future work is to include compiling full 18 term range assessments for planar and spherical measurement modes before obtaining reference pattern measurements.

Acknowledgements. The authors gratefully acknowledge A.C. Newell, T. Eibert, and M. Dirix for their many very valuable insights.

Competing interests. This research received no specific grant from any funding agency, commercial or not-for-profit sectors. The authors report no conflict of interest.

References

1. **Parini CG, Gregson SF, McCormick J, Janse van Rensburg D and Eibert T** (2021) Theory and Practice of Modern Antenna Range Measurements, 2nd Expanded Edition, Volume 1, IET Electromagnetic Waves Series 55 ISBN 978-1-83953-126-2.
2. **Yaghjian AD** (1986) An overview of near-field antenna measurements. *IEEE Transactions on Antennas and Propagation* **34**(1), 30–45 Jan. doi: 10.1109/TAP.1986.1143727
3. **Hansen JE** (1988) *Spherical Near-field Antenna Measurements*. London, UK: IEE Electromagnetic Waves Series, 26 Peter Peregrinus Ltd.
4. **Gregson SF, McCormick J and Parini CG** (2023) Principles of Planar Near-Field Antenna Measurements, 2nd Edition, IET Electromagnetic Waves Series 53, ISBN 978-1-83953-699-1, July.
5. **Petre P and Sarkar TK** (1992) Planar near-field to far-field transformation using an equivalent magnetic current approach. *IEEE Transactions on Antennas and Propagation* **40**(11), 1348–1356. doi: 10.1109/8.202712
6. **Gregson SF and Parini CG** (2024) A Comparison of Near-Field to Far-Field Transformation Techniques for Use With Industrial Multi-Axis Robotic Antenna Measurement Systems, 2024 18th European Conference on Antennas and Propagation (EuCAP), Glasgow, United Kingdom, pp. 1–5, doi: 10.23919/EuCAP60739.2024.10501489.
7. **Rudge AW, Milne K, Olver AD and Knight P** (1982) The Handbook of Antenna Design, Vol. 1, IET Press, ISBN 0-906048-82-6.
8. **Frandsen A, Jensen F and Larsen FH** (1985) Spherical Near-Field Transformation Program with Probe Correction, Manual for Computer Program SNIFTD. *Ticra Engineering Consultants, Communications Systems and Antennas*. November.
9. **Yaghjian AD** (1977) Near-Field Antenna Measurements on a Cylindrical Surface: A Source Scattering-Matrix Formulation. *NBS Technical Note 696* Boulder, Colorado: US Department of Commerce. September.
10. **Gregson SF, Parini CG, Pyne B, Saito H and Tanaka K** (2022) Highly Efficient Near-Field to Far-Field Transform for Polar Near-Field Scanned Data, AMTA, Denver Colorado, October.
11. **Hassett K, and Schluper B** (2024) Distributed RF Design Implementation for a Multi-functional Robotic Antenna Measurement System. *2024 Antenna Measurement Techniques Association Symposium (AMTA), Cincinnati*, OH, USA, October 2024.

Professor Stuart F. Gregson has 30 years of experience working in the space, aerospace, and communication sectors and is Director of Operations and Research at Next Phase Measurements, and a visiting professor at QMUL. He has BSc & MSc degrees in Physics from the University of Portsmouth and a PhD in near-field antenna measurements from QMUL. He has special experience with near-field antenna measurements, CEM, installed antenna & radome performance prediction, CATR design & simulation, EM scattering, 5G OTA measurements, and has published numerous peer-reviewed papers on these topics winning several best paper awards and regularly organizes courses on antenna metrology. He was the lead author of *Principles of Planar Near-Field Antenna Measurements*, and co-author of *Theory and Practice of Modern Antenna Range Measurements*, both of which are in 2nd editions. He is a Fellow of AMTA, the IET and the IoP, and is a chartered Engineer and Physicist.

Professor Clive G. Parini, FREng. received the BSc (Eng) and PhD degrees from Queen Mary University of London UK (QMUL) in 1973 and 1976, respectively. Joined QMUL as Lecturer in 1977, promoted to Reader in 1990, Professor in 1999, and is currently Emeritus Professor of Antenna Engineering at QMUL. In 2009, he was elected a Fellow of the Royal Academy of Engineering for his contribution to antenna metrology. He has published over 500 papers on research topics including array mutual coupling, array beam forming, antenna metrology, microstrip antennas, millimeter-wave compact antenna test ranges, millimeter-wave integrated antennas, metamaterials, and on-body communications. In 2008, he co-authored the book entitled *Principles of Planar Near-Field Antenna Measurements*, now in its 2nd edition (2023) and in 2014 co-authored the book entitled *Theory and Practice of Modern Antenna Range Measurements*, also now in its 2nd edition (2021).

Dennis Lewis received his BS EE degree with honors from Henry Cogswell College and his MS degree in Physics from the University of Washington. He has worked at Boeing for 36 years and is recognized as a Technical Fellow, leading the enterprise antenna measurement capability for Boeing Test and Evaluation. Dennis holds 12 patents and is the recipient of the 2013 & 2015 Boeing Special Invention Award. He is a senior member of the IEEE and several of its technical societies including the Microwave Theory and Technology Society, the Antennas and Propagation Society and the Electromagnetic Compatibility Society. He is a Senior Member and past Vice President of the Antenna Measurements Techniques Association and chaired its annual symposium in 2012 & 2023. Dennis developed and taught a course on the Fundamentals of Measurement Science at North Seattle College and serves on their Technical Advisory Committee.

Wayne Cooper Graduated Metrology USAF 1981. Wayne has worked in metrology for 44 years and been at Boeing for 39 years. Currently, he is recognized as an Associate Technical Fellow in RF, microwave, and electromagnetics. Wayne has served as senior lead of the Boeing microwave metrology lab before becoming lead of Boeing's precision dual robotic antenna measurement laboratory. Wayne currently holds four patents in high frequency and ultrasonic.

https://doi.org/10.1017/S1759078725000157 Published online by Cambridge University Press